energies

Article

An Innovative H-Type Flux Switching Permanent Magnet Linear Generator for Thrust Force Enhancement

Ehsan Farmahini Farahani, Nick J. Baker * and Farshid Mahmouditabar

School of Engineering, Newcastle University, Newcastle Upon Tyne NE1 7RU, UK;
ehsan.farahani@newcastle.ac.uk (E.F.F.); farshid.mahmouditabar@newcastle.ac.uk (F.M.)
* Correspondence: nick.baker@newcastle.ac.uk

Abstract: In this paper, two H-type flux switching permanent magnet linear generators with outer-translator and inner-translator configurations are discussed and compared to a more conventional flux switching topology. The stators consist of H-Type modules housing circumferential coils and are surrounded by two annular permanent magnets. In conventional flux switching machines, the windings are orientated perpendicular to the direction of motion and the conductors twist around the magnets. In H-type topologies, the orientation of the windings is in the same plain as the magnets and parallel to the direction of motion, resulting in an increase in flux linkage. The proposed topologies are designed for a low operating speed and a large magnetic gap, as found in wave energy converters. All topologies are optimized using the Taguchi optimization approach with the goals of reducing force ripple and increasing the average thrust force and efficiency. The 2D finite element method (FEM) is used in the optimization stage to calculate the optimized parameters of the presented generators, after which the optimized structures are simulated using 3D FEM, and the results are extracted. The results of the optimization show that the H-type topologies deliver a 20% higher shear stress whilst offering an easier to assemble structure.

Keywords: permanent magnet; flux switching generator; finite element analysis; Taguchi optimization method

Citation: Farahani, E.F.; Baker, N.J.; Mahmouditabar, F. An Innovative H-Type Flux Switching Permanent Magnet Linear Generator for Thrust Force Enhancement. *Energies* **2023**, *16*, 5976. https://doi.org/10.3390/en16165976

Academic Editors: João Filipe Pereira Fernandes, Paulo Jose Da Costa Branco, Silvio Vaschetto, Antonio Morandi and Jordi-Roger Riba Ruiz

Received: 2 July 2023
Revised: 25 July 2023
Accepted: 2 August 2023
Published: 14 August 2023

1. Introduction

As a result of the increased use of fossil fuels, the quantity of greenhouse gases is rising dramatically, which will result in an increase in global warming. Countries around the world are investigating low carbon electricity production, and wave energy is a potential solution. Internationally, several academic and industrial groups are looking at the development of wave energy converters. In the last decade, several technologies have been demonstrated at the kW and 100's of kW stage. The nature of the devices differs considerably, but many result in a low-speed oscillating motion that is not ideally suited to conventional electric machine topologies, which offer high efficiency at high speeds [1,2]. Hence, many concepts have intermediate mechanical links between the Wave Energy Converter (WEC) and the electric power take off. Recent research suggests using magnetic gear instead of the traditional mechanical gearbox, and several new topologies have been developed to boost the magnetic gearbox's (MGs) output torque. Reference [3] proposes a novel topology with Halbach PM array, which offers about 92% higher torque density than the conventional structure. Another MG with double layer spoke type PM array has been suggested in [4], and the results confirm that the proposed topology outperforms the conventional structure.

Direct drive linear generators are great candidates to convert the wave energy into electricity without the need to first convert the reciprocating motion to rotational motion. Electric machine topologies suitable for this application should have high force density, as, inevitably, this energy source operates at low speeds. This naturally leads the designer of the machine to investigate permanent magnet topologies, and flux switching variants specifically (e.g., [5]).

1.1. Linear Electric Machines for Wave Energy

Recently, research has been conducted, and some new topologies have been proposed to increase the force density of linear generator concepts. The permanent magnet Vernier hybrid machines (PMVHMs) utilize magnetic gearing to exhibit high force density at low speeds. In [6], the authors propose a cylindrical PMVHM, which offers about 20% higher force density compared to flat cross-section motors. Two novel topologies of vernier linear generator with V-type and inset rectangular-type PMs are proposed in [7], and they are compared in several aspects for use within wave energy converters. It was proven that the proposed V-type topology outperforms its counterpart in terms of thrust force and power factor. In [8], the power factor of the PMVHM was improved using the auxiliary DC field excitation, but, despite having a high force density, PMVHMs have a poor power factor. Reference [9] introduces a power control algorithm with a dual inverter to increase the power factor of PMVHMs.

To increase the power density of the linear generator, new topologies of transverse flux PM machines (TFPMs) have been suggested in several studies [10,11]. However, TFPMs have some inherent disadvantages, such as a low power factor, a complex structure, and the requirement for many small PMs. Permanent magnet assisted switched reluctance machines (PMSRMs) offer higher force or torque density than conventional switched reluctance machines (SRMs). In [12], the authors proposed a multi-tooth PM assisted SRM in which the PMs are placed between the stator C-core modules. The operating principle of the proposed topology in [12] is akin to the rotary motors proposed in [13–15]. The flux of the embedded PMs increases the air-gap flux density when one phase is excited, which results in a rise in force density. In [16], divided teeth SRM was proposed, and it was shown that as the number of teeth increases, the output torque increases as a result. Several topologies of flux switching permanent magnet machines (FSPMs) were suggested in recent articles as excellent candidates, since they provide high force/torque density and low torque ripple. In the airgap, the magnetic flux density of FSPM is roughly sinusoidal. A modular tubular FSPM linear generator (FSPMLG) is suggested [17] to improve the performance of the generator in comparison to the traditional structure. In [18], a novel E-type FSPMLG has been presented. The proposed topology has been optimized to improve the back emf waveform and reduce the cogging force of the generator. The proposed FSPMLG in [19] benefits from hybrid excitation. Some DC superconducting excitations are added to the proposed structure, and the results show that with hybrid excitation, the proposed topology produces higher trust force and lower cogging force. In [20], three double-sided PM synchronous linear generators (PMSLG) with parallel, Halbach, and axial array are proposed and compared in several aspects. The results show that the suggested generator with axial array has greater efficiency and a lower total mass than its competitors. A tubular superconducting flux-switching linear generator (TSFSLG), which can significantly enhance the performance of this type of generator, is proposed in [21]. The results proved that the proposed topology outperforms the conventional topology in terms of efficiency, power density, and cogging force. In [22], a multi-tooth flux-switching linear generator (MTFSLG) was suggested, and it was proven that the multi-tooth structure offers lower force ripple and cogging force as well as higher efficiency than the conventional structure.

1.2. Requirements of Linear Power Take off in Wave Energy Converters

In this work, the authors start from the perspective of what the fundamental requirements and constraints of power taken off in a wave energy converter are rather than idealized electric machine focused optimization. In large scale WECs, oscillations of several m's might need accommodation by machines with long active lengths assembled in a modular structure. Tight tolerances are unlikely. Furthermore, the translator and stator will need to withstand the marine environment, and so they are likely to be encapsulated. In linear configurations, the lubrication could be by way of solid contact bearings. All these factors imply optimizing electrical machines for small magnetic airgaps is not realistic. In this work, the authors start from the perspective of what the fundamental requirements and constraints of power taken off in a wave energy converter are, rather than idealized electric machine focused optimization. In large-scale WECs, oscillations of several m's might need accommodation by machines with long active lengths assembled in a modular structure. For example, [23] describes a rectangular cross-section generator with a peak power of 2 MW and a stroke length of 7 m, [24] discusses a 1 m diameter tubular machine rated at 1 kW with an active length of around 1.5 m, and [25] shows a 75 kW 2 m active length and 3 m stroke length linear machine. Tight tolerances at these sizes are unlikely, and to accommodate this, in [24], a 5 mm air gap is assumed. Furthermore, the translator and the stator will need to withstand the marine environment, and so they are likely to be encapsulated. In linear configurations, the lubrication could be by way of solid contact bearings. All of these factors imply that optimizing electrical machines for small magnetic air gaps is not realistic.

In this paper, a novel H-type flux switching permanent magnet linear generator (FSPMLG) is proposed. The proposed topology could have an outer-translator or inner-translator structure. To accurately compare and illustrate the capabilities of the proposed topology compared to conventional FSPMLG, a sequential Design of Experiment (DOE) based multi-level Taguchi method is implemented.

2. Machine Topology

The proposed outer-translator FSPM linear generator, FSPMLG (G1), is shown in Figure 1a. The stator is composed of six H-type modules, each housing circumferential armature windings and encompassed by two oppositely magnetized PMs. The windings of the two modules are connected in series to form one phase, as shown by their color. The proposed outer topology's translator embraces the stator and is the same as that of conventional LFSPMs without any flux resources. The active length contains eleven poles on the translator. Figure 1b shows the inner-translator variation of the H-type topology. The inner translator type operates on a similar premise as the outer translator type, with the distinction that the translator is situated in the middle of two stator components. The conventional FSPMLG is also shown in Figure 1c, which has similar pole combinations as the two suggested structures. In the conventional structure, the windings are twisted around the stator poles, and the PMs are implanted in the middle of the stator poles. To better show the structure of the proposed topologies, the 2D schematic of G1 and G2 along with the design parameters are illustrated in Figure 2. The main parameters of the presented FSPMLG are listed in Table 1. The support width ($W_{support}$) is set to a fixed value of 20 mm during the optimization process. Furthermore, the length of the PM (L_{pm}) and the area of the winding ($A_{winding}$) can be determined as follows:

$$L_{pm} = \frac{W_t}{2} - W_{ty} - H_{tt} - L_g - \frac{W_{support}}{2} \tag{1}$$

$$A_{winding} = \left(\frac{W_t}{2} - W_{ty} - H_{tt} - L_g - W_{sy} - \frac{W_{support}}{2}\right) * \left(\frac{L_a}{6} - 2 * W_{sp} - W_{pm}\right) \tag{2}$$

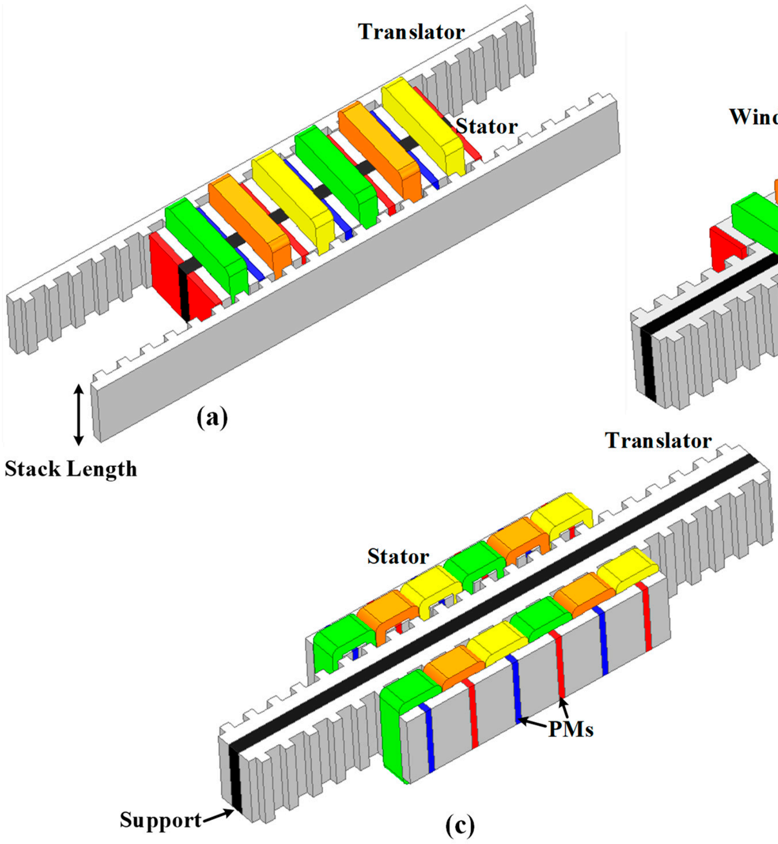

Figure 1. 3D schematics of the presented topologies (**a**) external-FSPMLG (G1), (**b**) internal-FSPMLG (G2), and (**c**) conventional FSPMLG (G3).

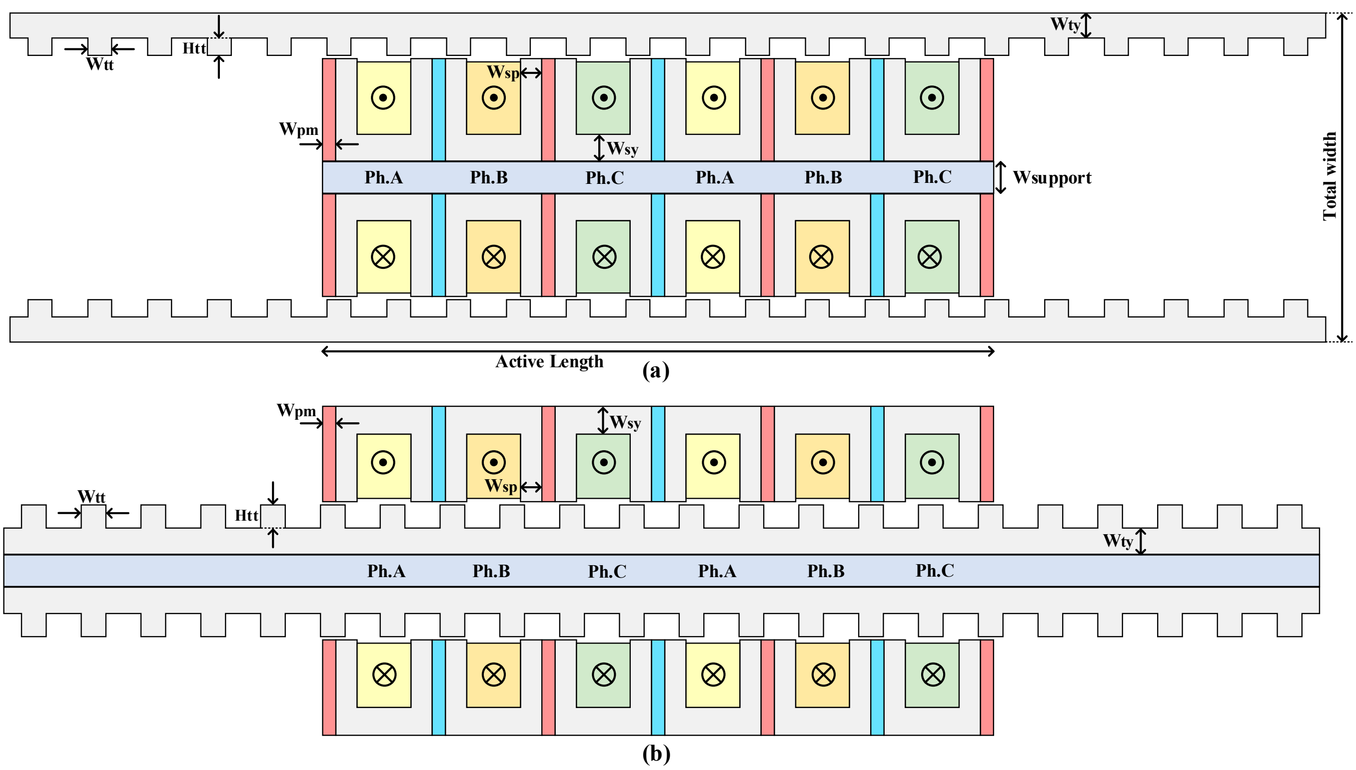

Figure 2. 2D structure and optimization parameters of the proposed generator (**a**) outer-translator FSPMLG (**b**) inner-translator FSPMLG.

Table 1. The main parameters of the presented topologies.

Parameter (Unit)	Symbol	Value
Active length (mm)	L_a	400
Total width (mm)	W_t	200
Stack length (mm)	L_s	100
Air-gap length (mm)	L_g	2
Support width (mm)	$W_{support}$	20
Current density (A/mm^2)	J	6
Translator velocity (m/s)	V	1

So, the active length, total width, and support width are chosen as fixed values in the optimization process, while all of the other dimensions are variable. The current density is considered to be a constant value of 6 A/mm^2 throughout the optimization process. However, because the winding area varies, the current also does. The phase current can be calculated as follows:

$$I_{phase} = \frac{A_{winding} \times J \times S_f}{N_c} \tag{3}$$

where S_f and N_c are the winding fill factor and the number of coils per winding, respectively.

Operational Basics

Figure 3 illustrates the simplified flux plot of the H-type topology at various mover positions. As seen in Figure 3a, in position 1, the red PM's flux travels through the translator back iron of the depicted phase in the right manner and closes its path. The flux linkage of the designated phase has therefore attained its highest positive value. The flux linkage of the given phase is at its most negative value when the translator moves to the right and shifts from position 1 to position 2, where it flows in the negative direction through the stator yoke of the same phase. The EMF is induced in the winding as the flux linkage shifts in accordance with the mover positions.

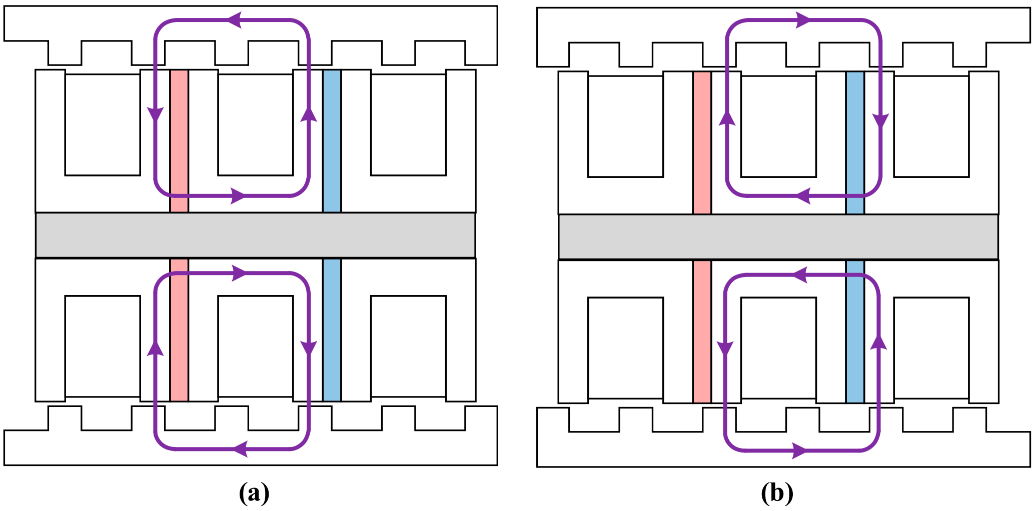

Figure 3. PMs' flux path of the presented structure: (**a**) position 1, (**b**) position 2.

3. Design Optimization

The utilized DOE-based optimization procedure for design optimization of two novel topologies of outer-translator and inner-translator H-type FSPMG and conventional FSPMG is illustrated in Figure 4. The details of the utilized optimization procedure are as follows.

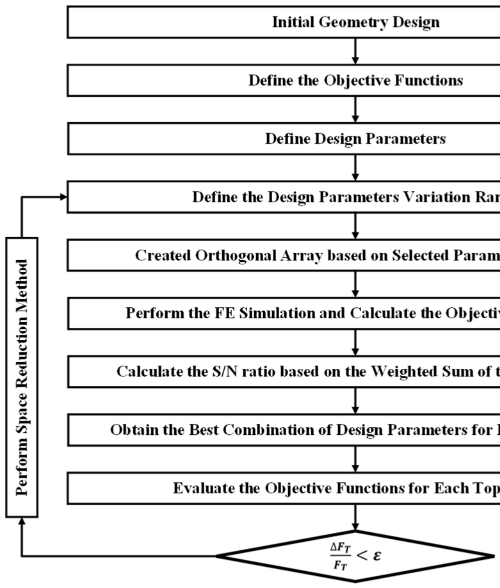

Figure 4. The flowchart of Taguchi optimization procedure.

3.1. Objective Function

Considering the special requirements of linear generator applications, the thrust force, force ripple, and efficiency of the machine are considered as optimization objectives. The weighted sum approach is utilized to convert the multi-objective optimization problem to a single-objective optimization problem, as stated in Equation (4). The coefficients of ω_1, ω_2, and ω_3 are considered 0.5, 0.3, and 0.2, respectively.

$$F_t(i) = \omega_1 \frac{F_{avg}(initial)}{F_{avg}(i)} + \omega_2 \frac{F_{ripple}(i)}{F_{ripple}(initial)} + \omega_3 \frac{F_{efficiency}(initial)}{F_{efficiency}(i)} \tag{4}$$

$$F_{ripple}(i) = \frac{F_{max}(i) - F_{min}(i)}{F_{avg}(i)} \tag{5}$$

$$F_{efficiency}(i) = \frac{P_{out}(i)}{P_{out}(i) + P_{Fe}(i) + P_{Cu}(i)} \tag{6}$$

where F_{max}, F_{min}, F_{avg}, P_{out}, P_{Fe}, and P_{Cu} are the maximum thrust force, minimum thrust force, average thrust force, output power, core loss, and copper loss of the generator, respectively.

3.2. Calculation of the S/N Ratio

An important factor in Taguchi optimization is the signal to noise (*S/N*) ratio that measures the effect of noise on each experiment. The method aims to optimize the experiments by reducing the noise effect. In this optimization method, the best combination of the design parameters is chosen to reduce the effect of the noise factors without changing or eliminating them. The *S/N* ratio for an experiment is calculated based on different optimization goals. In this paper, the optimization goal of F_{ave} and $F_{efficiency}$ is maximization while the goal of F_{ripple} is minimization. As stated in Equation (7), since the weighted sum is utilized to convert the MO problem to an SO problem, the target is to minimize the $F_t(i)$, resulting in the maximization of F_{ave} and $F_{efficiency}$ and the minimization of F_{ripple}. Therefore, the utilized equations for minimization (smaller is better) is as in Equation (7).

$$S/N = -10 \log\left(\sum_{i=1}^{n} \frac{{y_i}^2}{n}\right) \tag{7}$$

where n is the number of repeats in each experiment, and where y_i is the output of the experiment in i-th repeat.

3.3. Implementation of the Taguchi Method

The Taguchi optimization methods based on DOE require a low number of FEM simulation to obtain the optimum point. DOE is a statistical method for analysis of the experimental results [26]. The main advantage of the DOE-based design optimization procedure is the lower number of required FE models. In all three topologies, the considered design parameters are H_{tt}, W_{PM}, W_{sp}, W_{sy}, W_{tt}, *and* W_{ty} that are shown in Figure 2. The parameters have five levels and are presented in Table 2, as shown in Figure 2. There are two types of DOE partial-factor design and full-factor design. In this paper, in order to reduce the number of required FEM samples, the partial factor design was carried out using Orthogonal Array (OA). The OAs are predefined tables, and the rows present the combination of design variables whilst the objective values are presented in the column; the columns of the arrays are balanced and orthogonal [27]. This means that in each pair of columns, all factor combinations occur the same number of times. Orthogonal designs estimate the effect of each factor on the objectives independently of all other factors [28]. In the case of full factorial design, and considering five levels for each design parameter, the required FEM samples are 5^6 = 15,625, whereas to implement the Taguchi optimization method using OA, the predefined table of $L_{25}(5^6)$, as illustrated in Table 3, is utilized, where 25 is the number of required FEM samples.

Table 2. The considered levels of design parameters.

Parameter	Level 1	Level 2	Level 3	Level 4	Level 5
H_{tt} (mm)	10	11	12	13	14
W_{pm} (mm)	8	9	10	11	12
W_{sp} (mm)	13	14	15	16	17
W_{sy} (mm)	14	15	16	17	18
W_{tt} (mm)	13	14	15	16	17
W_{ty} (mm)	14	15	16	17	18

Table 3. The considered OA and calculated objective functions.

Run	H_{tt}	W_{PM}	W_{sp}	W_{sy}	W_{tt}	W_{ty}	F_{G1}(I)	F_{G1}(II)	F_{G1}(III)	F_{G2}(I)	F_{G2}(II)	F_{G2}(III)	F_{G3}(I)	F_{G3}(II)	F_{G3}(III)
1	11	11	15	18	15	30	0.793	1.004	0.989	0.814	0.956	0.997	0.906	1.052	1.010
2	11	12	16	19	16	31	0.835	1.108	1.031	0.819	1.014	1.020	0.871	1.181	1.082
3	11	13	17	20	17	32	0.902	1.232	1.080	0.884	1.136	1.067	0.919	1.303	1.141
4	11	14	18	21	18	33	1.043	1.391	1.150	1.006	1.269	1.116	1.092	1.411	1.199
5	11	15	19	22	19	34	1.183	1.559	1.216	1.151	1.419	1.185	1.253	1.603	1.273
6	12	11	16	20	18	34	0.960	1.066	1.030	0.928	1.001	0.989	1.002	1.111	1.036
7	12	12	17	21	19	30	1.053	1.173	1.071	1.047	1.068	1.030	1.125	1.259	1.124
8	12	13	18	22	15	31	1.123	1.320	1.126	1.109	1.172	1.090	1.170	1.383	1.194
9	12	14	19	18	16	32	1.239	1.453	1.190	1.236	2.158	1.143	1.206	1.476	1.244
10	12	15	15	19	17	33	0.891	1.188	1.070	0.863	1.062	1.034	0.999	1.227	1.120
11	13	11	17	22	16	33	1.147	1.136	1.062	1.082	1.027	1.032	1.171	1.209	1.117
12	13	12	18	18	17	34	1.248	1.242	1.105	1.178	1.155	1.053	1.229	1.324	1.191
13	13	13	19	19	18	30	1.525	1.390	1.156	1.556	1.271	1.143	1.612	1.478	1.244
14	13	14	15	20	19	31	0.999	1.123	1.050	1.003	1.044	1.029	1.034	1.234	1.107
15	13	15	16	21	15	32	1.051	1.267	1.102	1.132	1.151	1.068	1.089	1.327	1.189
16	14	11	18	19	19	32	1.478	1.205	1.083	1.498	1.122	1.053	1.454	1.247	1.101
17	14	12	19	20	15	33	1.651	1.318	1.141	1.584	1.184	1.092	1.642	1.407	1.234
18	14	13	15	21	16	34	1.095	1.090	1.029	1.079	1.018	1.012	1.103	1.202	1.098
19	14	14	16	22	17	30	1.249	1.231	1.081	1.271	1.097	1.044	1.225	1.304	1.135
20	14	15	17	18	18	31	1.384	1.345	1.133	1.480	1.232	1.091	1.406	1.375	1.197
21	15	11	19	21	17	31	2.224	1.273	1.123	2.198	1.188	1.068	2.101	1.342	1.128
22	15	12	15	22	18	32	1.223	1.054	1.023	1.207	0.979	0.987	1.295	1.137	1.053
23	15	13	16	18	19	33	1.351	1.140	1.059	1.349	1.033	1.028	1.386	1.244	1.128
24	15	14	17	19	15	34	1.531	1.305	1.123	1.477	1.177	1.101	1.472	1.397	1.203
25	15	15	18	20	16	30	2.123	1.447	1.187	2.168	1.292	1.142	1.964	1.519	1.271

Another important aspect of the Taguchi method is that it can be easily implemented in statistical software and provides the optimal combination of design parameters with a very small number of simulations. If evolutionary processing methods, such as Artificial Neural Network (ANN), Kriging Model (KM), etc., were used, the number of required simulations would increase greatly [29,30].

3.4. Space Reduction Method

One of the drawbacks of the Taguchi method is the limited levels of the design parameters variation. To improve the Taguchi method, space reduction methods can be utilized. Therefore, in a multi-level optimization procedure, the variation ranges of the design parameters are modified at each level. For example, considering the allowable variation range of the design parameter [a, b] and five levels for each parameter, if the optimum value of the Taguchi is equal to x_t, the new variation range of the parameter A is as Equation (8):

$$\left\{\begin{array}{cc} (a,\ a+d_i,\ a+2d_i,\ a+3d_i, a+4d_i) & x_t-2d_i<a \\ (b-4d_i,\ b-3d_i, b-2d_i, b-d_i, b) & x_t+2d_i>b \\ (x_t-2d_i, x_t-d_i,\ x_t, x_t+d_i, x_t+2d_i) & others \end{array}\right\} \tag{8}$$

where d_i is the distance between two levels. In each step of the utilized multi-level optimization procedure, the value of step size is halved. The multi-level optimization procedure is continued until the difference between the calculated objective function (F_T) of the k + 1 and k levels ($\frac{\Delta F_T}{F_T}$) are lower than $\varepsilon = 1\%$. The calculated weighted sum of each design combination is presented in Table 3. The index of I, II, and III in the title of each column corresponds to the iteration of optimization. For example, $F_{G2}(II)$ means the calculated weighted sum of the G2 topology at iteration 2.

3.5. Optimization Results

In the Taguchi method, the best level of each factor is corresponded to the one that has the highest *S/N* ratio. The results of *S/N* ratios for each iteration of studied FSPMGs are presented in Figure 5. The defined parameters level of each iteration is also presented in Table 4. The average *S/N* ratio of a level of a parameter can be calculated based on Equation (9) and Table 3. For example, to calculate the average *S/N* Ratio for the first level of the W_{PM}, consider the second column of Table 3. The average *S/N* ratio corresponding to level one is calculated by averaging according to Equation (9):

$$\overline{S/N}(W_{PM}, 1) = \frac{S/N(1) + S/N(6) + S/N(11) + S/N(16) + S/N(21)}{5\ (Number\ of\ levels)} \tag{9}$$

The best design level of each optimization variable corresponds to the level with the highest *S/N* ratio. For instance, in iteration 1 of the optimization, the optimum level of the design parameters are as follows:

Outer-translator FSPMLG (G_1): $H_{tt}(level\ 1 = 10), W_{PM}(Level\ 2 = 9), W_{sp}(Level\ 1 = 13), W_{sy}(level\ 5 = 18), W_{tt}(level\ 1 = 13), and\ W_{ty}(level\ 3 = 16)$.

Inner-translator FSPMLG (G_2): $H_{tt}(level\ 1 = 10)$, $W_{PM}(Level\ 2 = 9)$, $W_{sp}(Level\ 1 = 13)$, $W_{sy}(level\ 5 = 18)$, $W_{tt}(level\ 1 = 13)$, $and\ W_{ty}(level\ 5 = 18)$.

Conventional FSPMLG (G_3): $H_{tt}(level\ 1 = 10)$, $W_{PM}(Level\ 4 = 11)$, $W_{sp}(Level\ 1 = 13)$, $W_{sy}(level\ 5 = 18)$, $W_{tt}(level\ 2 = 14)$, $and\ W_{ty}(level\ 3 = 16)$.

After obtaining the optimum levels of iteration 1, it is necessary to use Equation (8) to reduce the design parameters variation range and halve the step size. For example, in iteration 2, the step size of the design parameters is reduced from 1 mm to 0.5 mm. This procedure is continued until the convergence occurs. The results indicate that after three iterations, all three designs converged. The optimum levels of the design parameters at each iteration are highlighted in bold in Table 4. The calculated weighted sum objective functions of different topologies are presented in Figure 6.

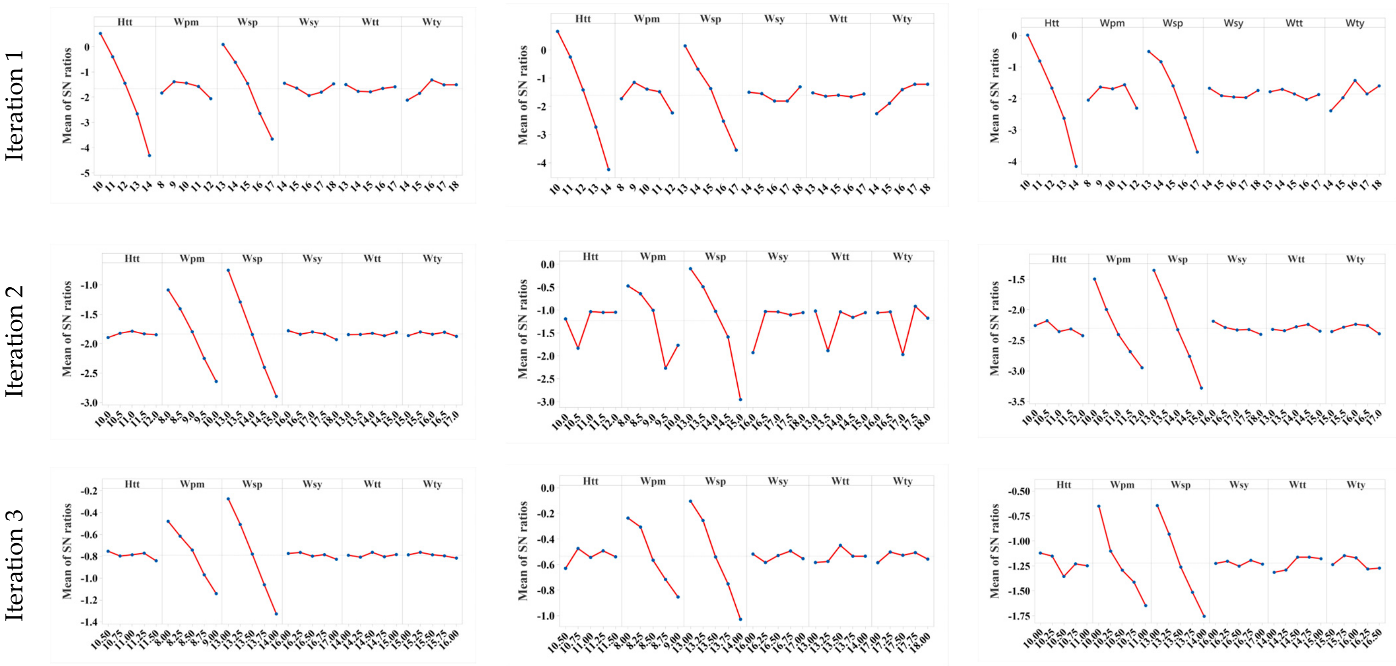

(**a**) (**b**) (**c**)

Figure 5. The calculated means and *S/N* ratios: (**a**) outer-translator (G1), (**b**) inner-translator (G2), and (**c**) conventional (G3).

Table 4. The considered levels of design parameters at each iteration.

Topology		**Outer Translator FSPMG**					**Inner Translator FSPMG**					**Conventional FSPMG**				
	Parameter	**I**	**II**	**III**	**IV**	**V**	**I**	**II**	**III**	**IV**	**V**	**I**	**II**	**III**	**IV**	**V**
Iteration 1	H_{tt} (mm)	**10**	11	12	13	14	**10**	11	12	13	14	**10**	11	12	13	14
	W_{pm} (mm)	8	**9**	10	11	12	8	**9**	10	11	12	8	9	10	**11**	12
	W_{sp} (mm)	**13**	14	15	16	17	**13**	14	15	16	17	**13**	14	15	16	17
	W_{sy} (mm)	14	15	16	17	**18**	14	15	16	17	**18**	14	15	16	17	**18**
	W_{tt} (mm)	**13**	14	15	16	17	**13**	14	15	16	17	13	**14**	15	16	17
	W_{ty} (mm)	14	15	**16**	17	18	14	15	16	17	**18**	14	15	**16**	17	18
Iteration 2	H_{tt} (mm)	10	10.5	**11**	11.5	12	10	10.5	**11**	11.5	12	10	**10.5**	11	11.5	12
	W_{pm} (mm)	**8**	8.5	9	9.5	10	**8**	8.5	9	9.5	10	**10**	10.5	11	11.5	12
	W_{sp} (mm)	**13**	13.5	14	14.5	15	**13**	13.5	14	14.5	15	**13**	13.5	14	14.5	15
	W_{sy} (mm)	**16**	16.5	17	17.5	18	16	**16.5**	17	17.5	18	**16**	16.5	17	17.5	18
	W_{tt} (mm)	13	13.5	14	14.5	**15**	**13**	13.5	14	14.5	15	13	13.5	14	**14.5**	15
	W_{ty} (mm)	15	**15.5**	16	16.5	17	16	16.5	17	**17.5**	18	15	15.5	**16**	16.5	17
Iteration 3	H_{tt} (mm)	**10.5**	10.75	11	11.25	11.5	10.5	**10.75**	11	11.25	11.5	**10**	10.25	10.5	10.75	11
	W_{pm} (mm)	**8**	8.25	8.5	8.75	9	**8**	8.25	8.5	8.75	9	**10**	10.25	10.5	10.75	11
	W_{sp} (mm)	**13**	13.25	13.5	13.75	14	**13**	13.25	13.5	13.75	14	**13**	13.25	13.5	13.75	14
	W_{sy} (mm)	16	**16.25**	16.5	16.75	17	16	16.25	16.5	**16.75**	17	16	16.25	16.5	**16.75**	17
	W_{tt} (mm)	14	14.25	**14.5**	14.75	15	13	13.25	**13.5**	13.75	14	14	14.25	**14.5**	14.75	15
	W_{ty} (mm)	15	**15.25**	15.5	15.75	16	17	**17.25**	17.5	17.75	18	15.5	**15.75**	16	16.25	16.5

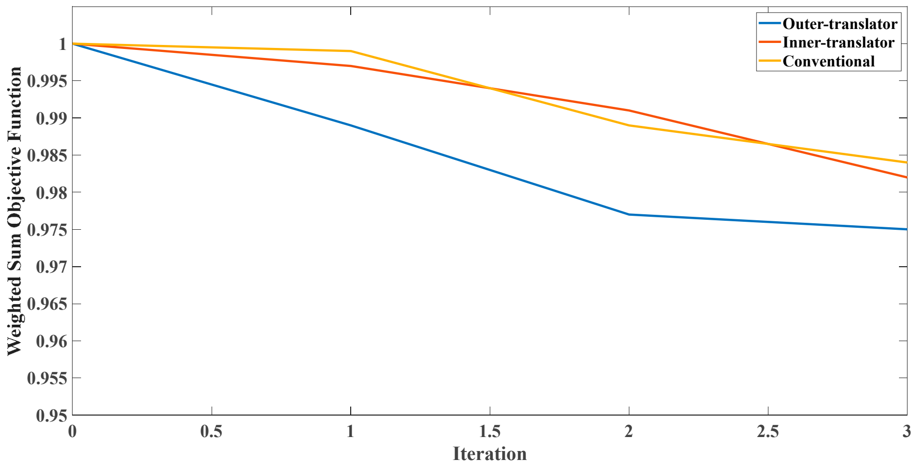

Figure 6. The progress of the calculated weighted sum objective functions of different topologies.

4. Simulation Results

The flux lines of the presented designs are illustrated in Figure 7, which authenticates the operating principles of the proposed topologies. The magnetic flux density distributions of the presented topologies are obtained at the nominal current density of 6 A/mm^2 to investigate the saturation behaviors of the presented designs, as shown in Figure 8. At the rated current density, all designs have proper condition in term of saturation, and the magnetic flux density value inside the translator and stator teeth is approximately 1.8 T, near the knee point of the ferromagnetic steel, and just some small parts of the translator and stator teeth are saturated.

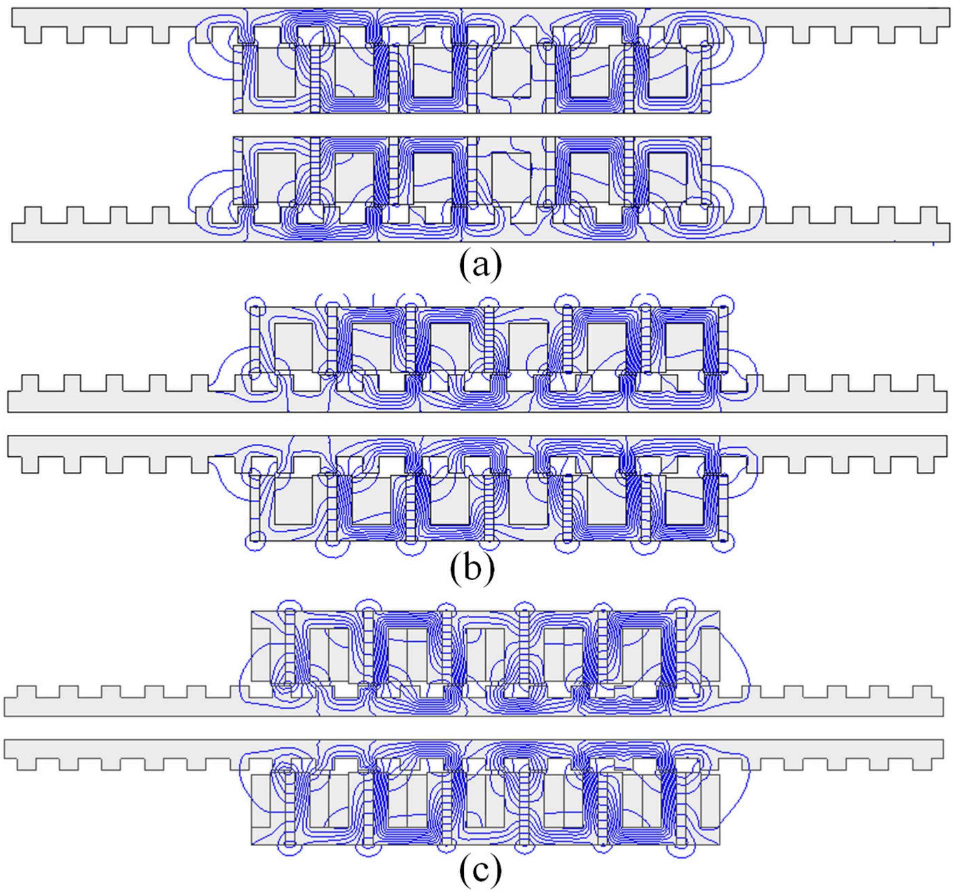

Figure 7. Flux line patterns of the presented FSPMLGs (**a**) outer- translator (G1), (**b**) inner-translator (G2), and (**c**) conventional (G3).

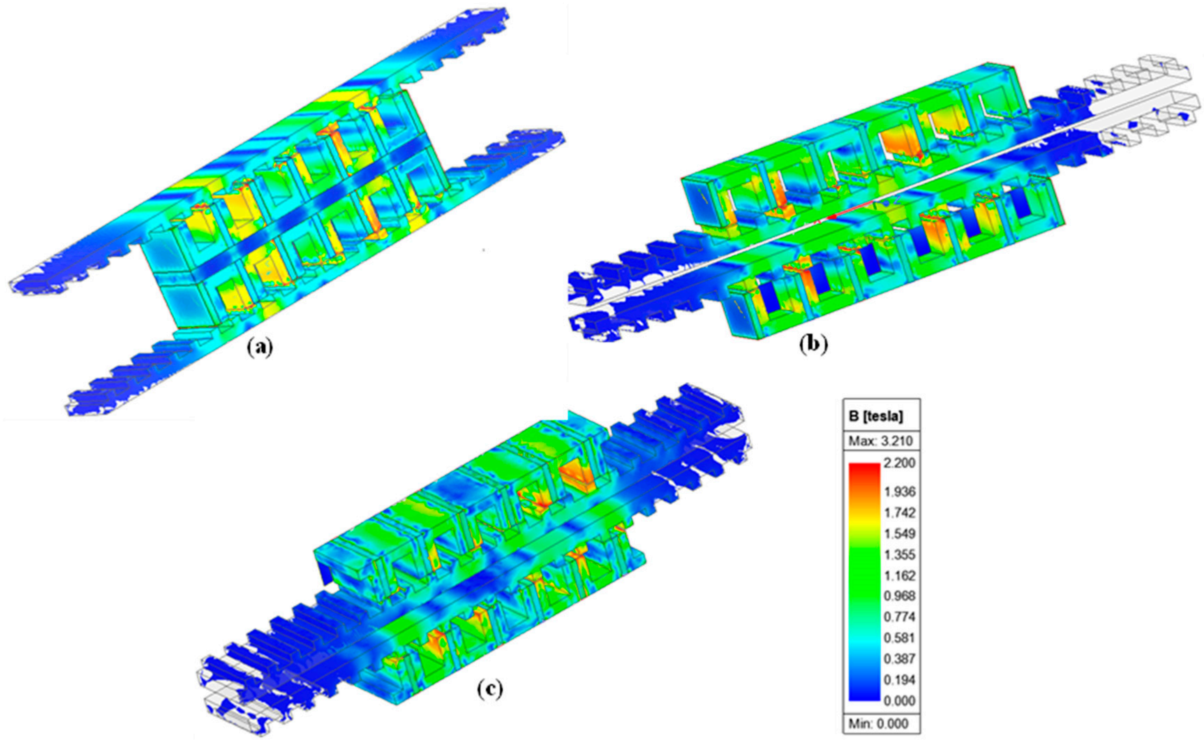

Figure 8. Magnetic flux density distributions of the presented FSPMLGs (**a**) outer-translator (G1), (**b**) inner-translator (G2), and (**c**) conventional (G3).

The thrust force profiles of the optimum designs of the presented topologies are shown in Figure 9. The proposed outer-translator FSPMLG (G1) and inner-translator FSPMLG (G2) topologies produce higher thrust force than the conventional FSPMLG (G3) structure with the same size and current density. The thrust forces produced by G1, G2, and G3 are 2987, 2971, and 2490 N, respectively. It should be noted that the average thrust force of G1 and G2 are approximately equal, and they are 19.9% higher than that of the conventional structure. Additionally, the force ripples of G1, G2, and G3 are 18.43%, 19.03%, and 24.2%, respectively. So, the H-type outer-translator FSPMLG offers the lowest thrust force ripple among the presented topologies.

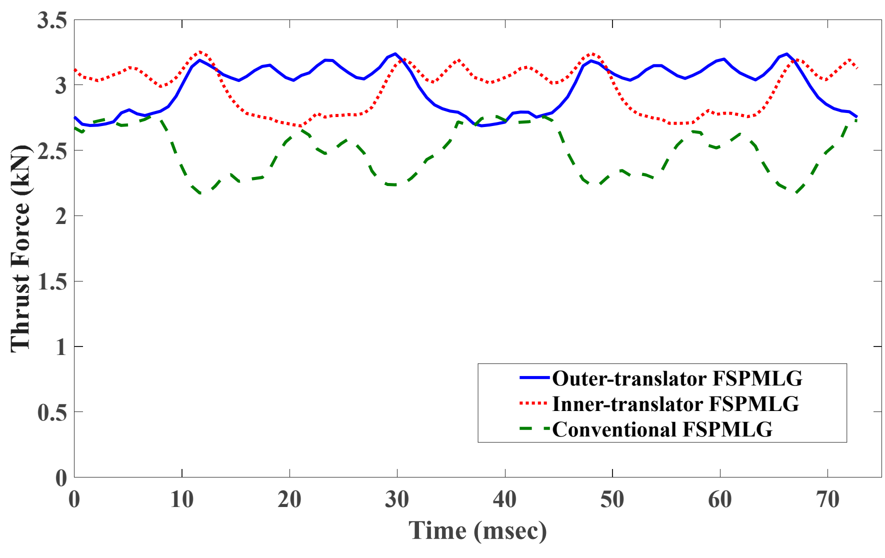

Figure 9. Thrust force curves of the presented FSPMLGs.

The waveform of a single-phase back emf of all the topologies at the nominal speed of 1 m/s are plotted in Figure 10. All designs have 50 turns per slot. It can be observed that the back emf amplitude of G1 and G2 are approximately equal, which is about 32.9% greater than that of G3.

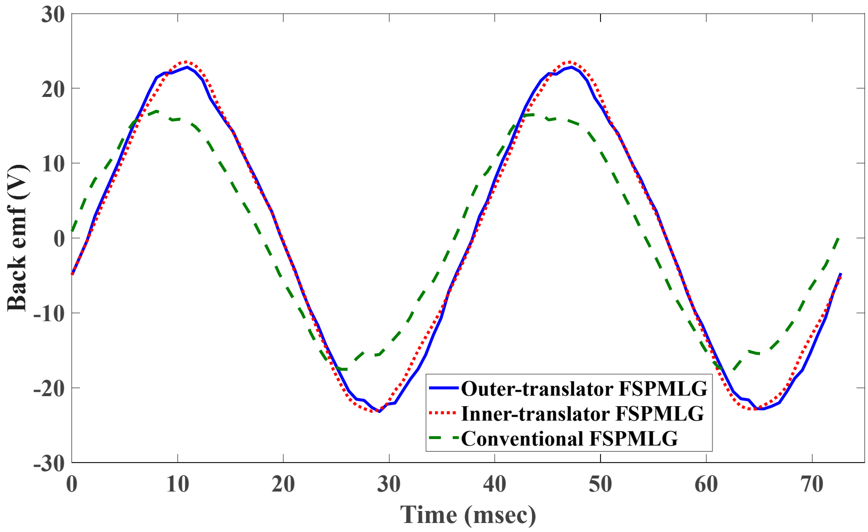

Figure 10. Back emf curves of the presented FSPMLGs.

5. Discussion of H Type Topology

In this section, the fundamental difference between the H type and the more conventional flux switching machines is discussed. In all of the presented topologies, the active part of the coil is perpendicular to the direction of motion. In the H-type configuration, the end winding is also perpendicular to the direction of motion, whereas in the conventional layout, G3, the end winding is parallel to the motion. The H type FSM can be described as circumferentially wound, and it is more easily adaptable to a cylindrical cross section version as compared to the more conventional single tooth winding type FSM. It has also been shown to have better performance.

5.1. Performance and Operation

For a better comparison, the results of the proposed topologies and the conventional structure are listed in Table 5. The output power can be calculated by multiplying the thrust force by the operating velocity; for example, if all of the machines are driven at 1 m/s, the output powers of G1, G2, and G3 would be 2987, 2971, and 2490 W, respectively. Furthermore, the efficiency values of G1, G2, and G3 are calculated as 90.4%, 90.8%, and 89.6%, respectively, at the rated current density of 6 A/mm^2 and the rated speed of 1 m/s.

Table 5. Results comparison of the presented topologies at the speed of 1 m/s.

Parameter	Outer Translator (G1)	Inner Translator (G2)	Conventional (G3)
Thrust force (N)	2986.5	2970.5	2490.1
Average shear stress (kN/m^3)	37.33	37.13	31.12
Force ripple (%)	18.43	19.03	24.2
Output power (W)	2986.5	2970.5	2490.1
Copper loss (W)	287	269.8	266.9
Hysteresis loss (W)	28.7	27.4	19.9
Eddy current loss (W)	2.5	2.3	1.6
Total iron loss (W)	31.2	29.7	21.5
Power factor	0.511	0.508	0.403
Efficiency (%)	0.9037	0.9084	0.8962

The increase in power is driven by the increase in force reacted. Fundamentally, the circumferential winding version of this machine can react to a larger force within the same volume envelope with the same magnet mass, and it is subjected to the same MMF. This stems from the fact that the flux flow from the magnet is better utilized in this version, demonstrated by the 27% increase in peak open circuit flux as stated in Figure 11. This can be qualitatively explained by examining the flux plot.

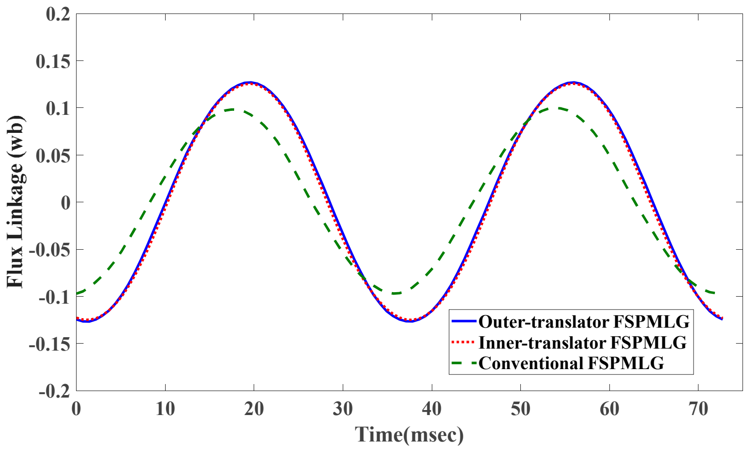

Figure 11. The comparison of open circuit flux of different topologies.

As shown in Figure 12, the orientation of the fundamental flux linking the coils for the two machines is 90 degrees apart. For the conventional FSM, the flux linkage is vertical in the plane of the paper, and for the circumferential machine, it is horizontal across the page. Figure 13 shows the FEA flux plot for the peak flux linkage position, annotated with the main and leakage fluxes, the direction of the remnant flux in the magnets, and the area of flux linkage driving the back emf.

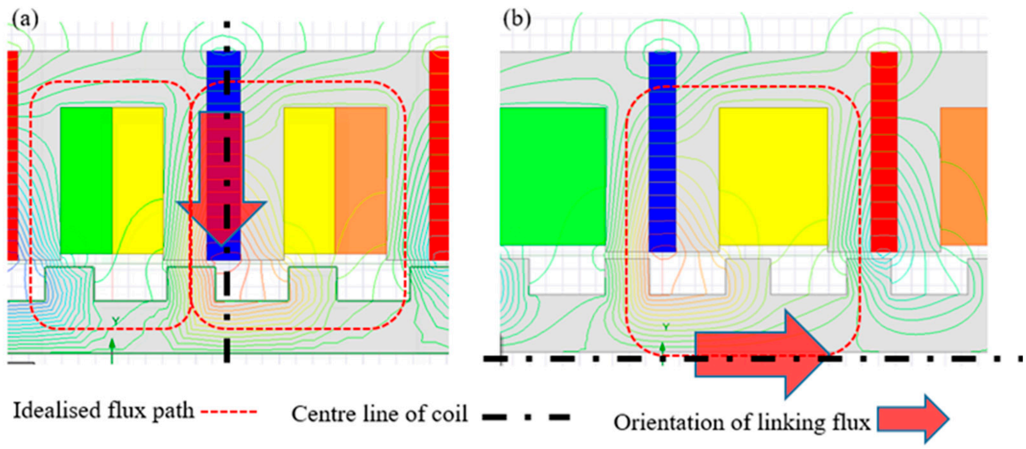

Figure 12. The orientation of the fundamental flux linking the coils, which will generate the back emf for the (**a**) conventional and (**b**) circumferential coil versions.

The reluctance network and the flux paths are fundamentally the same in the two machines. The net flux linkage is the net flow bound by the coil. In both machines, the magnitude of the main flux, shown as a green arrow, is offset by a leakage return path. The leakage consists of tooth leakage (shown in black) and slot leakage (shown in blue). In the conventional wound FSM, the slot leakage actively opposes the main flux path, whereas in the circumferential machine, the slot leakage does not link the coil. The net linkage in the circumferentially wound machine is therefore greater, resulting in a higher back emf and a higher force capability.

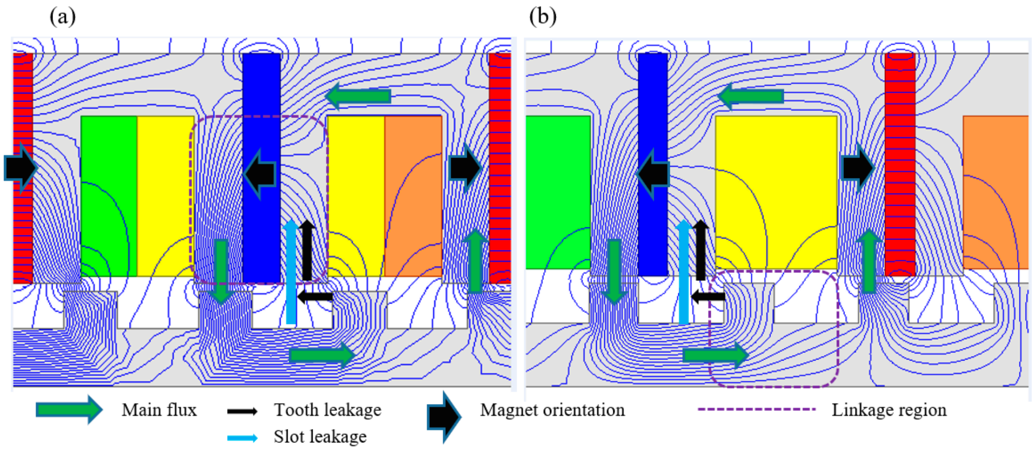

Figure 13. FEA flux plot of the optimized topologies, annotated for (**a**) conventional and (**b**) proposed topology at the maximum flux position, zero current.

5.2. Cylindrical Variants and Manufacturing Issues

The analysis in this work has been 2D, assuming a flat cross section and ignoring any losses in the end windings. However, in many applications, a cylindrical cross section is beneficial, and numerous cylindrical machines have been demonstrated to be simple to manufacture (for example, [31]).

Any of the three topologies studied here could be made in a cylindrical variant. The conventional single tooth winding version, G3, would have to consist of a number of teeth equally spaced around the circumference. Figure 1c showed the end winding and the active part of the winding. The cylindrical variant of G3 would need space for the end windings, and Figure 14 shows an example of a cylindrical linear machine, developed in [5], which consists of three single tooth windings. The end windings are highlighted as running in the direction of motion, axially into the plain of the figure. They contribute to the I^2R losses, but they do not contribute to the force developed. In addition, as shown in Figure 14, provision for the end windings results in a loss of active area. Configuration G3 is therefore not well suited for a cylindrical variant.

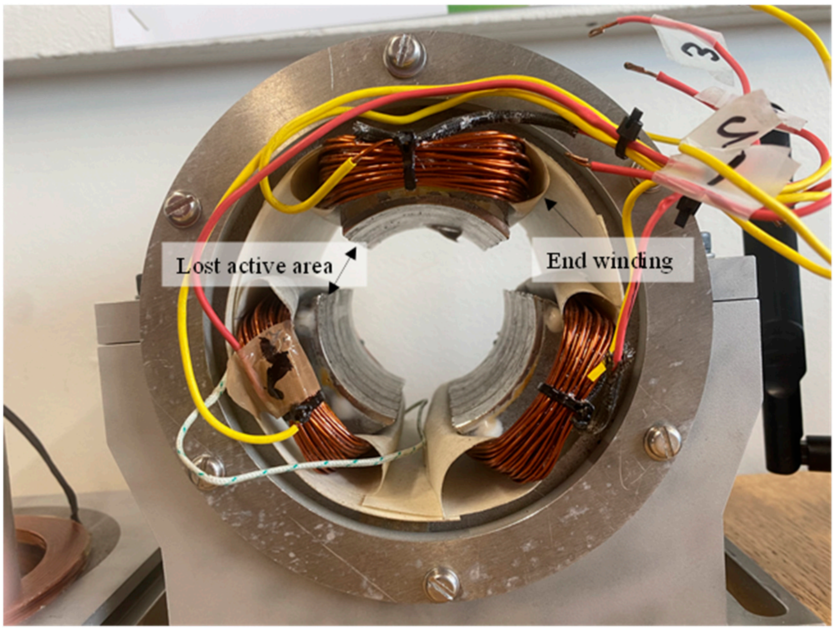

Figure 14. An example of circumferential wound machine assembled by stacking concentric coils, teeth, and core back.

Cylindrical variants of topologies G1 and G2 would both be circumferential windings. All of the copper contributes to force production in this case, and there are no end windings. The cylindrical versions of outer-translator and inner-translator H-Type FSPMLG are presented in Figure 15a,b, respectively. The circumferential wound machine can be assembled by stacking concentric coils, teeth, and core back, as illustrated in Figure 15c. In this instance, the steel 'H' is made from three stacked components, and both variants are therefore well suited to cylindrical variants. It should also be noted that in Figure 14, the windings are wrapped around the stator teeth, which leads to active area decrement. However, in the proposed tubular topology, which is shown in Figure 15, the windings can be circumferential. To prototype the proposed tubular topology, material such as SMC should be utilized. The difference of the new topology with the topology of Figure 14 relates to the current path rather than the flux path. In Figure 14, the current is circumferential and axial, whereas in Figure 15, the current is circumferential only.

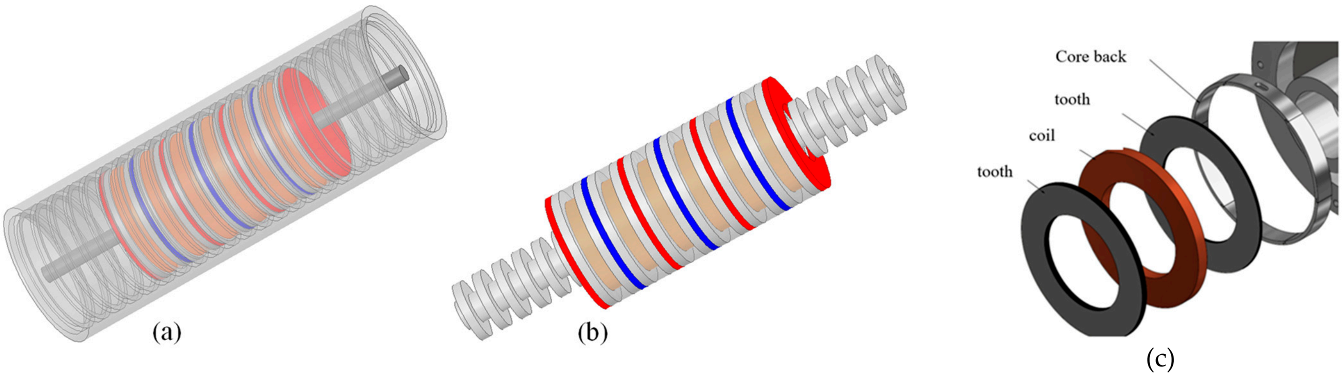

Figure 15. (**a**) The cylindrical outer-translator H-Type FSPMLG G1 (**b**) the cylindrical inner-translator H-Type FSPMLG G2, and (**c**) the manufacturing process of G2, consisting of circumferential windings assembled by stacking concentric coils, teeth, and core back.

6. Conclusions

This study offers two new H-type FSPM linear generators for use in wave energy converters with outer-translator and inner-translator configurations, and it compares performance to a conventional flux switching design. The key difference with the H-type configuration is that the end winding is perpendicular to the direction of motion, which has an impact on the flux linkage.

The stator in the proposed outer-translator FSPMLG is made up of six H-type modules, and the armature windings are wound around the H-bridges whilst the PMs are inserted between the neighboring modules. We have discussed how this topology's straightforward structure makes it simple to produce, particularly if a cylindrical topology is required. The H-type inner-translator topology is conceptually identical to the outer-translator topology, other than that the translator is placed between the two parts of the stator.

The main parameters of the proposed topologies and the conventional flux switching structure are obtained using the basic equations of electric machines, assuming a current density of 6 A/mm^2, an operating speed of 1 m/s, and an assumed magnetic gap of 2 mm. Each topology has been optimized using the sequential multi-level Taguchi method, and the results acquired using 3D FEM. The outer-translator and inner-translator topologies have about equal average thrust forces, which are higher by around 20% than the thrust forces of the conventional structure. This improved performance is because of the orientation of the coils. Additionally, compared to the inner-translator and conventional structures, the outer-translator topology's force ripple is roughly 0.6% and 5.77% lower, respectively.

Author Contributions: Conceptualization, E.F.F. and N.J.B.; Investigation, E.F.F. and F.M.; Writing—original draft, E.F.F., F.M. and N.J.B.; Supervision, N.J.B.; Funding acquisition, N.J.B. All authors have read and agreed to the published version of the manuscript.

Funding: This research was funded by Engineering and Physical Sciences Research Council grant number EP/V040758/1.

Conflicts of Interest: The authors declare no conflict of interest.

References

1. Farrok, O.; Islam, M.R.; Sheikh, M.R.I.; Guo, Y.; Zhu, J.G. A Split Translator Secondary Stator Permanent Magnet Linear Generator for Oceanic Wave Energy Conversion. *IEEE Trans. Ind. Electron.* **2018**, *65*, 7600–7608. [CrossRef]
2. Rodriguez, L.G.-T.; Lafoz, M.; Torres, J.J.; Obradors, D.; Blanco, M.; Najera, J.; Navarro, G.; Garcia, F.; Sanchez, A. New Type of Linear Switched Reluctance Generator for Wave Energy Applications. *IEEE Trans. Appl. Supercond.* **2020**, *30*, 1–5. [CrossRef]
3. Jing, L.; Wang, T.; Tang, W.; Liu, W.; Qu, R. Characteristic Analysis of the Magnetic Variable Speed Diesel–Electric Hybrid Motor with Auxiliary Teeth for Ship Propulsion. *IEEE/ASME Trans. Mechatron.* **2023**. [CrossRef]
4. Jing, L.; Liu, W.; Tang, W.; Qu, R. Design and Optimization of Coaxial Magnetic Gear with Double-Layer PMs and Spoke Structure for Tidal Power Generation. *IEEE/ASME Trans. Mechatron.* **2023**. [CrossRef]
5. Baker, N.J.; Almoraya, A.; Raihan, M.A.H.; McDonald, S.; McNabb, L. Development and Wave Tank Demonstration of a Fully Controlled Permanent Magnet Drive for a Heaving Wave Energy Converter. *Energies* **2022**, *15*, 4811. [CrossRef]
6. Baker, N.J.; Raihan, M.A.H.; Almoraya, A.A. A Cylindrical Linear Permanent Magnet Vernier Hybrid Machine for Wave Energy. *IEEE Trans. Energy Convers.* **2019**, *34*, 691–700. [CrossRef]
7. Almoraya, A.A.; Baker, N.J.; Smith, K.J.; Raihan, M.A.H. Design and Analysis of a Flux-Concentrated Linear Vernier Hybrid Machine with Consequent Poles. *IEEE Trans. Ind. Appl.* **2019**, *55*, 4595–4604. [CrossRef]
8. Ching, T.W.; Chau, K.T.; Li, W. Power Factor Improvement of a Linear Vernier Permanent-Magnet Machine Using Auxiliary DC Field Excitation. *IEEE Trans. Magn.* **2016**, *52*, 1–4. [CrossRef]
9. Xu, D.; Zhao, W.; Cheng, Y.; Chen, Q.; Xu, L. Power factor improvement of permanentmagnet linear vernier motor by using dualinverter with hybrid discontinuous PWM. *IET Power Electron.* **2019**, *12*, 3438–3446. [CrossRef]
10. Qiu, S.; Zhao, W.; Zhang, C.; Shek, J.K.H.; Wang, H. A Novel Structure of Tubular Staggered Transverse-Flux Permanent-Magnet Linear Generator for Wave Energy Conversion. *IEEE Trans. Energy Convers.* **2022**, *37*, 24–35. [CrossRef]
11. Chen, M.; Huang, L.; Hu, M.; Hu, B.; Ahmad, G. A Spiral Translator Permanent Magnet Transverse Flux Linear Generator Used in Direct-Drive Wave Energy Converter. *IEEE Trans. Magn.* **2021**, *57*, 1–5. [CrossRef]
12. Vatani, M.; Ghaffarpour, A.; Kondelaji, M.A.J.; Mirsalim, M. Study of a Modular Toothed Linear Hybrid Reluctance Motor with Permanent Magnets in Translator Slots. *IEEE Trans. Transp. Electrif.* **2022**, *8*, 3554–3567. [CrossRef]
13. Kondelaji, M.A.J.; Farahani, E.F.; Mirsalim, M. Teethed-Pole Switched Reluctance Motors Assisted with Permanent Magnets: Analysis and Evaluation. *IEEE Trans. Energy Convers.* **2021**, *36*, 2131–2140. [CrossRef]
14. Radmanesh, H.; Farahani, E.F. Performance evaluation of a new modular split-tooth permanent magnet-assisted switched reluctance motor. *IET Electr. Power Appl.* **2022**, *17*, 441–451. [CrossRef]
15. Farahani, E.F.; Mirsalim, M. Comprehensive study on divided-teeth and permanent magnet assisted outer-rotor switched reluctance motors. *IET Electr. Power Appl.* **2020**, *14*, 2293–2300. [CrossRef]
16. Farahani, E.F.; Kondelaji, M.A.J.; Mirsalim, M. Divided Teeth Switched Reluctance Motor with Different Tooth Combinations. In Proceedings of the 2020 11th Power Electronics, Drive Systems, and Technologies Conference, PEDSTC 2020, Tehran, Iran, 4–6 February 2020. [CrossRef]
17. Yan, L.; Li, W.; Jiao, Z.; Hu, H.; Chen, C.Y.; Chen, I.M. Design and modeling of tubular flux-switching permanent magnet linear motor. In Proceedings of the 2014 IEEE Chinese Guidance, Navigation and Control Conference, CGNCC 2014, Yantai, China, 8–10 August 2014; pp. 2799–2804. [CrossRef]
18. Huang, L.; Yu, H.; Hu, M.; Zhao, J.; Cheng, Z. A novel flux-switching permanent-magnet linear generator for wave energy extraction application. *IEEE Trans. Magn.* **2011**, *47*, 1034–1037. [CrossRef]
19. Huang, L.; Hu, M.; Liu, J.; Yu, H.; Zeng, C.; Chen, Z. Electromagnetic Design of a 10-kW-Class Flux-Switching Linear Superconducting Hybrid Excitation Generator for Wave Energy Conversion. *IEEE Trans. Appl. Supercond.* **2017**, *27*, 1–6. [CrossRef]
20. Seo, S.W.; Jang, G.H.; Kim, J.M.; Choi, J.Y. Characteristic Analysis and Experimental Verification for a Double-Sided Permanent Magnet Linear Synchronous Generator According to Magnetization Array. *IEEE Trans. Appl. Supercond.* **2018**, *28*, 1–4. [CrossRef]
21. Huang, L.; Liu, J.; Yu, H.; Qu, R.; Chen, H.; Fang, H. Winding configuration and performance investigations of a tubular superconducting flux-switching linear generator. *IEEE Trans. Appl. Supercond.* **2014**, *25*, 1–5. [CrossRef]
22. Cai, J.; Lu, Q.; Huang, X.; Ye, Y.; Fang, Y. Performance investigation of a novel multi-tooth switched-flux linear motor. In Proceedings of the 2015 10th International Conference on Ecological Vehicles and Renewable Energies, EVER 2015, Monte-Carlo, Monaco, 31 March–2 April 2015. [CrossRef]
23. Polinder, H.; Damen, M.E.C.; Gardner, F. Linear PM generator system for wave energy conversion in the AWS. *IEEE Trans. Energy Convers.* **2004**, *19*, 583–589. [CrossRef]
24. Prudell, J.; Stoddard, M.; Amon, E.; Brekken, T.K.A.; Von Jouanne, A. A permanent-magnet tubular linear generator for ocean wave energy conversion. *IEEE Trans. Ind. Appl.* **2010**, *46*, 2392–2400. [CrossRef]

25. Burchell, J.; Ahmed, N.; Barajas-Solano, J.I.; Mueller, M.; Galbraith, M. Project Neptune: Critical Component Tests for a Fully Flooded Direct-Drive Linear Generator for Wave Energy Convertors. In Proceedings of the 4th Asian Wave and Tidal Energy Conference, Taipei, Taiwan, 13 September 2018.
26. Mahmouditabar, F.; Vahedi, A.; Takorabet, N. Demagnetisation optimisation of ring winding axial flux permanent magnet motor by modifying the load line of the magnet. *IET Electr. Power Appl.* **2023**, *17*, 928–938. [CrossRef]
27. Mahmouditabar, F.; Vahedi, A.; Takorabet, N. Robust Design of BLDC Motor Considering Driving Cycle. *IEEE Trans. Transp. Electrif.* **2023**. [CrossRef]
28. Mahmouditabar, F.; Vahedi, A.; Takorabet, N. Design and Analysis of Interior Permanent Magnet Motor for Electric Vehicle Application Considering Irreversible Demagnetization. *IEEE Trans. Ind. Appl.* **2022**, *58*, 284–293. [CrossRef]
29. Asanuma, J.; Doi, S.; Igarashi, H. Transfer Learning through Deep Learning: Application to Topology Optimization of Electric Motor. *IEEE Trans. Magn.* **2020**, *56*, 1–4. [CrossRef]
30. Mahmouditabar, F.; Vahedi, A.; Mosavi, M.R.; Bafghi, M.H.B. Sensitivity analysis and multiobjective design optimization of flux switching permanent magnet motor using MLP-ANN modeling and NSGA-II algorithm. *Int. Trans. Electr. Energy Syst.* **2020**, *30*, e12511. [CrossRef]
31. Korbekandi, R.M.; Baker, N.J.; Kulan, M.C.; Jalal, A.S.; Wu, D.; Li, M. Dynamic Characteristics and Demonstration of an Integrated Linear Engine Generator with Alternative Electrical Machines. *Energies* **2022**, *15*, 5295. [CrossRef]